A numerical study of concentrated photovoltaic-thermal (PV-T) solar collectors with spectral beam splitters

Chandan Pandey[a], Yong Yan Chai[a], Seiw Wen Ng[a], Sandesh S. Chaugule[a], Gan Huang[a,b] and Christos N. Markides[a*]

[a] Clean Energy Processes (CEP) Laboratory, Department of Chemical Engineering, Imperial College London, London, UK.
[b] Institute of Microstructure Technology, Karlsruhe Institute of Technology, Karlsruhe, Germany.
** Corresponding author: c.markides@imperial.ac.uk*

Abstract:

Concentrated hybrid photovoltaic-thermal (CPV-T) solar collectors can generate high-grade thermal energy and electricity simultaneously. The thermal energy output of conventional CPV-T-collectors are constrained by the operating temperatures of the solar cells employed in these collectors, whose temperature cannot exceed 70-90 °C. To overcome this limitation, new CPV-T- collector designs have been proposed and explored that feature spectral beam splitters (SBSs). A SBS acts as an optical filter which, for a CPV-T collector with silicon cells, allows wavelengths between 500-1100 nm to pass onto primary PV-T collector while reflecting the rest to a secondary thermal absorber. This optical filtering acts to reduce the operating temperature of the cells, thereby improving their electrical performance. The reflected rays from the SBS filter, which mostly consist of the UV and IR parts of the solar spectrum, are directed onto a secondary thermal absorber whose purpose is to extract high-grade thermal energy, thereby improving the potential of thermal energy extraction. In this work, SBS-based CPV-T collectors are explored. Ray-tracing simulations are performed to optimise the geometrical arrangement of the secondary thermal absorber and SBS, while computational fluid dynamics (CFD) modelling is used to compare the performance of such CPV-T collectors to that of collectors without a SBS. The effects of solar irradiance and inlet water temperature are studied in detail. Preliminary results show that for a solar incidence of 1000 W m^{-2}, the use of a SBS enables a 30-35 °C reduction in the solar cell operation temperature, leading to potential electrical efficiency benefits of ~22%.

Keywords:

Concentrated solar; Hybrid PV-thermal; Solar energy; Spectral beam splitting.

1. Introduction

Technologies that are capable of utilising renewable energy sources, such as wind and solar, have become noteworthy contributors to the global energy mix, accounting for 38% of the total electricity generation in 2022 [1]. The renewable electricity market has been mostly dominated by solar photovoltaic (PV) technologies, which account for ~27% of renewable electricity generation [1]. Solar PV technology directly converts solar energy to electricity by the photovoltaic effect [2]. Solar energy is also utilised for hot water and process heating applications by solar thermal technologies. The market for solar hot water systems was valued to be $ 4.7 billion in 2019 and is expected to reach 6.7 billion by 2027 [3].

Other than PV and solar thermal systems, hybrid PV-thermal (PV-T) collectors are also an available option. A PV-T collector combines PV cells with a thermal absorber and is thus capable of generating electrical and thermal energy simultaneously [4-6]. A PV-T collector has a higher energy density and occupies ~50 % less rooftop space compared to individual solar PV and solar thermal collectors [7-9]. However, one of the major challenges with conventional PV-T collectors concerns the low-grade nature of the thermal energy generated (~60 °C) [10]. To overcome this challenge, concentrated photovoltaic thermal (CPV-T) collectors have been proposed. CPV-T collectors typically consist of an additional component referred to as a concentrator, which collects part of the solar radiation and reflects this onto the PV-T modules [11-14].

The PV cells in such CPV-T collectors are commonly Si based [15]. Only photons with energy higher than the bandgap will be utilised for electricity conversion by the cells, while the excess spectrum incident on the cells will be dissipated as waste heat. This causes cell temperature to rise, especially under concentrated solar

irradiation. Consequently, the conversion efficiency can drop by as much as 0.004-0.006 K^{-1} [16]. To overcome this challenge, spectral beam splitting has been considered for hybrid PV-T collectors.

A spectral beam splitter (SBS) is used to split the incident solar spectrum by transmitting the electrically usable part of the spectrum to the PV cells for electricity generation, while directing the remaining spectrum to a secondary solar thermal absorber, allowing for more effective use of the incident solar irradiation [17]. Recently, various SBS concepts and designs have been developed, based on interference filters [18, 19] or liquid absorptive filters [20]. Interference filters, such as dichroic filters for CPV-T collectors are commonly thin multilayer materials with non-absorptive high or low refractivity [21]. The incident spectrum splits at the layer boundaries of the SBS where a specified bandwidth is reflected and the remaining transmitted.

Liquid absorptive filters have gained an interest in recent years compared to dichroic filters, particularly the use of nanofluids, since they can act as spectral splitters, carrier fluids for the thermal energy generated and coolants for the PV cells. While nanofluids offer multiple functions, further research is needed to enhance their stability under concentrated irradiance and high temperature [22]. In contrast, multilayer dichroic filters are more stable and do not degrade as easily [23].

This study aims to develop a coupled optical-thermal CFD model of a CPV-T collector which utilises a dichroic SBS and to evaluate the collector's performance under varying operational conditions. In this paper, Section 2 deals with numerical modelling for the CPV-T collector, and Section 3 presents validation results of the developed methodology followed by a sensitivity analysis to study the effects of different parameters on the collector performance. Finally, important conclusions are summarised in Section 4.

2. Methodology

2.1. SBS CPV-T solar collector description

The collector examined in this study is a concentrated photovoltaic-thermal (CPV-T) collector that consists of a parabolic solar concentrator, an SBS, a primary PV-T collector containing water as the heat transfer fluid (HTF), and a secondary thermal absorber. The geometrical configuration of the collector is shown in Figure 1. The concentrator is a reflector with a reflectivity of 0.90, where radiation from the sun is reflected. The reflected rays are then concentrated towards the SBS. The SBS splits the radiation into transmitted and reflected rays. The transmitted rays are further received by the primary PV-T module for electricity and thermal energy generation while the reflected rays are absorbed by the secondary thermal absorber for generating high-temperature thermal energy.

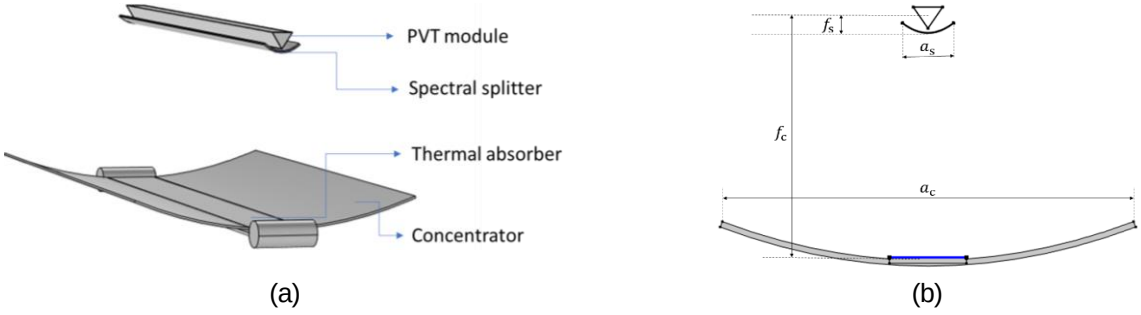

Figure 1. (a) CPV-T collector components, and (b) collector geometry.

2.2. Collector geometry

The length of the CPV-T collector is chosen to be 1 m. The cross-section view of the collector is shown in Figure 1. The distance between the concentrator, SBS and the triangular channel is determined according to the focal lengths of the concentrator and the SBS. The focal points of both the SBS and the parabolic concentrator fell at the centre of the triangular channel. The focal lengths of the concentrator (f_c) and SBS (f_s) are set at 420 mm and 25 mm, respectively. The aperture of the concentrator a_c and the SBS a_s are fixed at 670 mm and 84 mm, respectively. The thickness of all surfaces is set to 1 mm. The length of the CPV-T collector is chosen to be 1 m. The geometry of the collector is shown in Figure 1b. Since the collector was designed for silicon solar cells choosing a high concentration will result in overheating of the solar cells. To avoid this, the collector was designed for a geometrical concentration ratio of 6.2. A comparison of similar collector geometries that were studied before is presented in Table 1.

Table 1. Comparison of concentration ratio investigated in previous studies.

Study	Geometrical concentration ratio
Zhang et al. [19]	7
Peacock et al. [17]	10
Present work	6.2

The geometrical concentration ratio (*GCR*), optical concentration ratio (*OCR*) and optical efficiency (η_{opt}) of the collector are important optical characteristics of the collector geometry. The *GCR* is defined as the ratio of the area of the concentrator (A_c) to the area of the absorber (A_{cell}) [24]:

$$GCR = \frac{A_c}{A_{cell}} \quad (1)$$

while the *OCR* is defined as the ratio of the total incident flux on the PV cells (I_{cell}) to the total source flux, i.e., solar irradiation (I_0):

$$OCR = \frac{I_{cell}}{I_0} \quad (2)$$

The optical efficiency is defined as the OCR to GCR ratio:

$$\eta_{opt} = \frac{OCR}{GCR} \quad (3)$$

The *GCR*, *OCR* and optical efficiency of the collector in this study are 6.2, 5.6 and 0.9, respectively.

2.3. Computational modelling

COMSOL Multiphysics was used to analyse the geometrical optics and to evaluate the heat transfer and fluid flows in the CPV-T collector in Figure 1. Since the concentrator is a linear parabolic trough, the ray tracing simulations were performed in COMSOL Multiphysics with a three-dimensional (3-D) configuration. From the 3-D simulation, the solar flux reaching the primary PV-T module and the thermal absorbers are estimated. The ratio of flux reaching the primary PV-T module to the total flux available at the SBS is referred to as the transmission fraction. The transmitted fraction of the rays obtained through the 3-D geometrical optics simulation is then used to estimate the total flux reaching the solar cell. Similarly, the complement of transmission fraction is used to estimate the total flux reaching the secondary thermal absorber. Further, heat transfer across the solid and fluid domains as well as fluid dynamics is evaluated in the 3-D model through multiphysics coupling.

2.3.1. Optical model

A 3-D ray tracing model is developed to study ray propagation in the collector. A non-sequential ray-tracing approach is taken by COMSOL geometrical optics to solve for the ray propagation pathway of the geometry. The direction of ray propagation is constant until the path intersects with a boundary that separates two mediums with different refractive indices. Rays at a boundary can be either refracted, reflected, or absorbed.

For refracted rays, propagation from a boundary is determined by the refractive index of the ray propagation medium. The direction of the refracted ray is extrapolated out from a boundary according to Snell's law [25]:

$$n_1 \sin\theta_i = n_2 \sin\theta_t \quad (4)$$

where n is the refractive index, θ_i is the angle of incidence and θ_t is the angle of transmittance. The medium through which the rays propagate is indicated by subscripts '1' and '2'.

The speed at which the rays propagate through a medium (c) can be determined from:

$$c = \frac{c_o}{n} \quad (5)$$

where c_o is the speed of light and n is the refractive index of the material.

For reflected rays, the law of reflection which states that the angle of incidence is equal to the angle of reflectance is obeyed. The geometrical optics is evaluated with the assumption that the wavelength of the radiation is insignificant relative to the dimensions of the collector.

Light rays from the sun are simulated as polychromatic light with wavelengths in the range of 5 nm to 3000 nm. The concentrator is simulated as an illuminated boundary in the 3-D model. Boundary conditions are specified to model the filter property of the SBS. Rays with a wavelength range of 500-1100 nm are set to pass through the boundary while the remaining rays are reflected. The refractive index is defined as 1 for the SBS material. The refractive index value is dependent on the SBS material used. The reflection coefficient of the SBS is specified as 1. The properties of the SBS in this model are outlined in Table 2. Material discontinuities are specified at the outer surface of the SBS to exclude the release of reflected rays at these boundaries, which will contribute to stray light rays that produce noise in the result.

Table 2. Properties of the SBS in the model.

Property	Value
Transmitted wavelength	500-1100 nm
Refractive index	1
Reflection coefficient of the concentrator	0.9
Reflection coefficient of the SBS	1

2.3.2. 3-D CFD model

A 3-D model is developed to simulate heat transfer and fluid flow in the CPV-T collector. The absorption and conversion of the reflected rays into heat at the PV cells are represented in the model. Heat fluxes within the geometry are determined by considering heat transfer in the solid and fluid domains.

Light absorbed by a PV cell is converted into heat and electricity. The total radiation reaching the cell (S) is:

$$S = (I_0 A_{\text{cell}}) r_{\text{conc}} \tau_{\text{SBS}} \tag{6}$$

where r_{conc} is the reflectivity of the concentrator and τ_{SBS} is the transmitted fraction of the SBS. The value of τ_{SBS} was obtained through a geometrical optics simulation across the SBS.

The radiation reaching the PV cell is converted into electricity and heat. The heat generated in the cell (q) is:

$$q = S\alpha_{\text{PV}}(1 - \eta_{\text{PV}}) \tag{7}$$

where η_{PV} is the electrical efficiency and α_{PV} is the absorptivity of the PV cell. The heat generated is collected by the HTF in the duct.

The electrical efficiency of the PV cell (η_{PV}) depends on the PV cell temperature as follows [26-27]:

$$\eta_{\text{PV}} = \eta_0(1 - \beta(T_{\text{cell}} - 25\ ^\circ\text{C})) \tag{8}$$

where β is the power temperature coefficient and T_{cell} is the PV cell temperature. The base electrical efficiency (η_0) is the electrical efficiency at standard test conditions, i.e., a cell temperature maintained at 25 °C, I_0 is 1000 W m^{-2} and AM1.5G spectrum.

In the solid domain, thermal energy is transferred from the PV cell to the HTF via conduction. Heat transfer in the solid domain is governed by:

$$k_{\text{s}}\nabla^2(T_{\text{s}}) + q_{\text{s}} = 0 \tag{9}$$

where k_{s} is the thermal conductivity of the solid, T_{s} is the temperature of the solid domain and q_{s} is the heat generated in the solid domain. The thermal boundary condition at the PV cell is described by:

$$-\boldsymbol{n} \cdot q_{\text{out}} = q_0 \tag{10}$$

where n is the direction vector and q_{out} is the outward heat flux to the surroundings. These boundary conditions correspond to the convective heat flux to the surrounding and the surface-to-ambient radiation at the PV cell. For convection, q_{conv} is:

$$q_{\text{conv}} = h(T_{\text{amb}} - T) \tag{11}$$

where T_{amb} is the ambient temperature, T is the cell temperature, and h is the convective heat transfer coefficient, which is calculated from the correlation [11]:

$$h = 2.8 + 3w \tag{12}$$

where w is the surrounding wind speed in m/s. For the surface-to-ambient radiative flux, q_{rad}:

$$q_{\text{rad}} = \varepsilon\sigma({T_{\text{sky}}}^4 - T^4) \tag{13}$$

where ε is the cell surface emissivity, σ is the Stefan-Boltzmann constant, and T_{sky} is the sky temperature [11]:

$$T_{\text{sky}} = 0.0552{T_{\text{amb}}}^{1.5} \tag{14}$$

The inflow condition corresponds to the heat of the HTF at the inlet. The outflow condition is specified to account for convection-dominated heat transfer at the outlet. The thermal boundary conditions for inflow and outflow assigned to the fluid domain are given by:

$$-\boldsymbol{n} \cdot q_{\text{inlet}} = \rho_{\text{f}}\Delta h \boldsymbol{v_{\text{f}}} \cdot \boldsymbol{n} \tag{15}$$

$$-\boldsymbol{n} \cdot q_{\text{outlet}} = 0 \tag{16}$$

where q_{inlet} inflow heat flux, ρ_{f} the fluid density, $\boldsymbol{v_{\text{f}}}$ the fluid velocity, c_{p} the fluid heat capacity, T the immediate fluid temperature, T_{inlet} the fluid temperature at the inlet, and Δh is the specific enthalpy change defined by:

$$\Delta h = \int_{T_{\text{inlet}}}^{T} c_{\text{p}}\,\mathrm{d}T \tag{17}$$

For the fluid domain, the flow regime is determined using the Reynolds number (Re), defined by:

$$Re = \frac{\rho_{\text{f}} v d_{\text{h}}}{\mu} \tag{18}$$

where u is the fluid flow speed, d_{h} is the hydraulic diameter and μ is the dynamic viscosity. The hydraulic diameter is calculated from:

$$d_{\text{h}} = \frac{4A}{p} \tag{19}$$

where A is the cross-sectional area of the duct and p is the “wetted” perimeter of the duct. The critical Re for laminar flow in a triangular duct is 1100 [28].

Conservation of mass, momentum, and energy, are used to model the fluid flow:

$$\rho_{\mathrm{f}} \nabla \cdot \boldsymbol{v}_{\mathbf{f}} = 0 \tag{20}$$

$$\rho_{\mathrm{f}} \boldsymbol{v}_{\mathbf{f}} \nabla \cdot \boldsymbol{v}_{\mathbf{f}} = -\nabla P + \nabla \cdot \boldsymbol{\tau} + \rho_{\mathrm{f}} \mathrm{g} \tag{21}$$

$$\rho_{\mathrm{f}} c_{\mathrm{p}} \boldsymbol{v}_{\mathbf{f}} \nabla \cdot T_{\mathrm{f}} = \nabla \cdot (k_{\mathrm{f}} \nabla T_{\mathrm{f}}) \tag{22}$$

where P is the fluid pressure, τ is the viscous stress tensor, g is gravitational acceleration, T_{f} is the fluid temperature and k_{f} is the conductivity of the fluid. The fluid flow is assumed to be incompressible, in which the fluid density is expected to be constant with respect to time and space. The fluid is specified as a Newtonian fluid in which its dynamic viscosity is dependent on its thermodynamic state. This assumption is valid as the fluid in this collector is chosen to be water, which obeys the properties of a Newtonian fluid under normal conditions. For the fluid domain, a no-slip boundary condition is specified on the channel walls. The inflow boundary condition is given by the mass flow rate of the HTF.

2.4. Collector performance

The effects of solar irradiance and the mass flow rate of the HTF on the collector performance are examined by using the 3-D model. The outlet temperature of the HTF and maximum PV cell temperature are obtained from COMSOL. Collector performance with and without an SBS is also evaluated by setting the transmitted fraction of the SBS to 1 (for a non-SBS collector) and 0.57 (for an SBS-incorporated collector).

Here, the performance indicators of the collector are the PV cell efficiency, determined by Eq. (8), and the thermal efficiency of the HTF, determined by:

$$\eta_{\mathrm{th}} = \frac{\dot{m} c_{\mathrm{p}} \Delta T}{I_0 A_{\mathrm{c}}} \tag{23}$$

where $\dot{m}$ is the mass flow rate and ΔT is the temperature difference between the inlet and outlet of the HTF.

2.5. Mesh independent study

A mesh-independent study was also conducted on the model. For the simulation of the model, a physics-controlled mesh was used. The mesh sizes were varied from coarse to finer (options available in COMSOL). It was observed that the simulation did not converge for coarse mesh due to multiple physics involved in the simulation such as optics, heat transfer and fluid mechanics. Furthermore, when the mesh sizes were reduced to finer size with 271907 domain elements, the results were fairly accurate as presented in sections 3.1 and 3.2. When mesh elements were reduced to the extra fine, it was difficult to simulate the model due to the limited computational capacity of the workstation. Therefore, finer elements were chosen for this study.

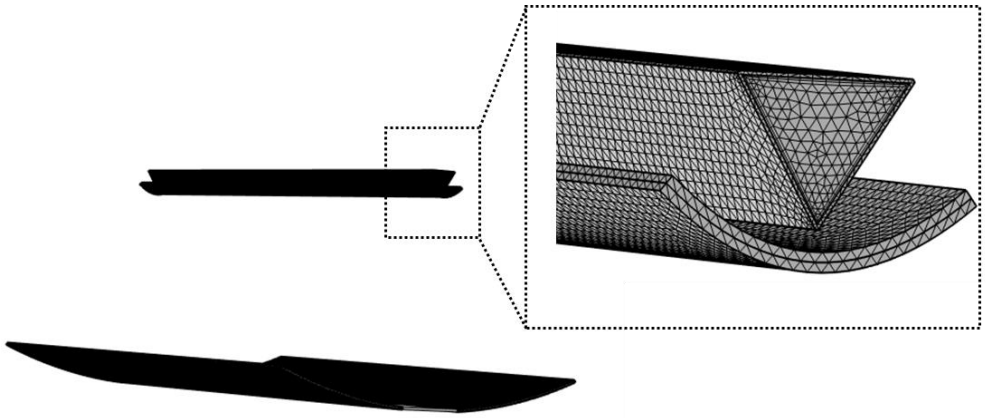

Figure 2. Meshed CPV-T collector.

3. Results and discussion

3.1. Validation of the spectral splitting optical model

The transmitted fraction (τ_{SBS}) of spectral splitter was calculated to validate the optical model of the collector of interest. The transmitted fraction of the spectrum through the convex SBS is defined as the ratio of flux transmitted to the primary PV-T module to the flux reaching the SBS boundary. The transmitted fraction for the convex SBS in this study is calculated to be 0.57. This value is similar to Zhang et al.'s value of 0.56 [19]. Further, to validate the optical model, the angular study of average optical flux falling on the absorber has also been validated against the work from Tang et al. [29], as shown in Figure 3. A close match between average concentration ratios is observed with a relative error under 1%.

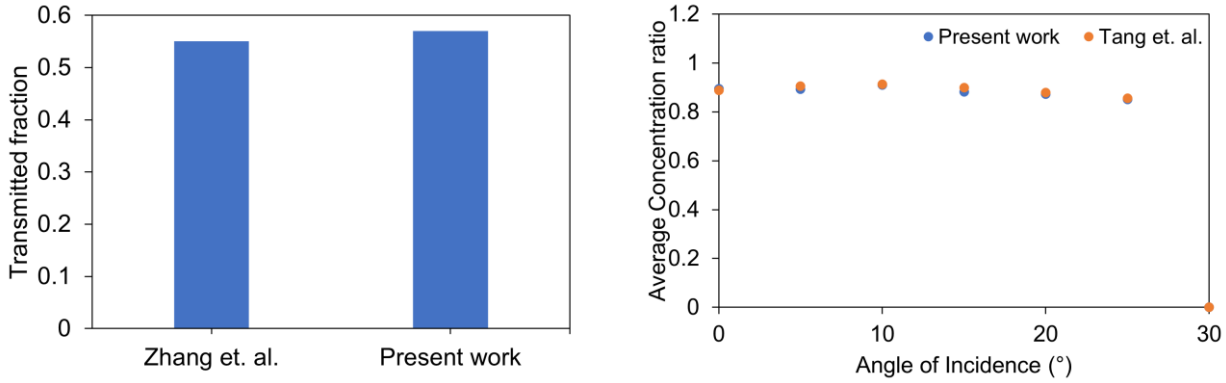

Figure 3. Optical model validation: (a) transmission fraction, and (b) average concentration ratio.

3.2. Validation of the coupled optical-electrical-thermal model

The coupled optical-thermal model can also be validated against the work from Bahaidarah et al. [30]. Simulations were performed for an unglazed compound parabolic concentrator integrated into a PV-T module for uncooled conditions. To estimate the cell temperature, parameters such as location, time, tilt angle, irradiance, ambient temperature, electrical efficiency at STC conditions and, wind speed have been used as inputs to the model. The parameters were varied at a time interval of 1 hour. Results show an acceptable match between the cell temperatures obtained from the experimental work of Bahaiderah et al. [30] and the current coupled optical, electrical and thermal model. The relative error is below 8%, as shown in Figure 4.

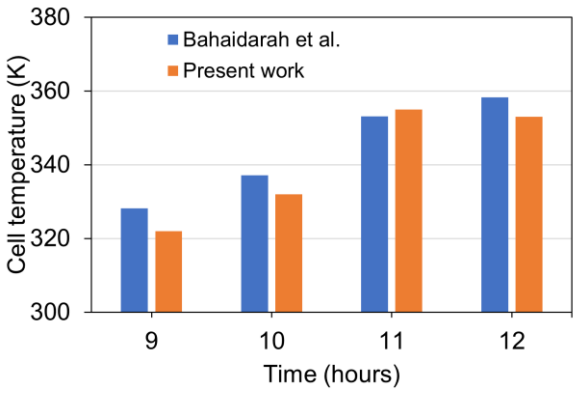

Figure 4. Optical-electrical-thermal model validation.

3.3. Optimisation of SBS filter configurations

The 3-D model for the SBS-CPV-T collector was used for geometrical optics simulation to select the optimum SBS configuration, which minimises optical losses, i.e., ray divergence. A convex and concave SBS are considered with a flat plate SBS as a control. As the SBS material is assigned a refractive index of unity, the transmitted rays through the upper SBS layer did not refract from their initial trajectories for all SBS configurations. For the reflected spectrum, the angle of reflection equals the angle of incidence. Thus, the reflected ray trajectory is dependent on the curvature of the bottom SBS layer, as shown in Figure 5.

The concave SBS resulted in the greatest optical loss with no rays received at the secondary thermal absorber, as shown in Figure 5a. The flat plate SBS demonstrated a focal point far from the thermal absorber, with some rays received by the thermal absorber, as shown in Figure 5b. The convex SBS is chosen as all reflected rays at the

layer boundary are directed onto the thermal absorber without any observable ray divergence, as shown in Figure 5c. The flux distribution on the top and bottom absorber for the convex splitter is shown in Figure 6.

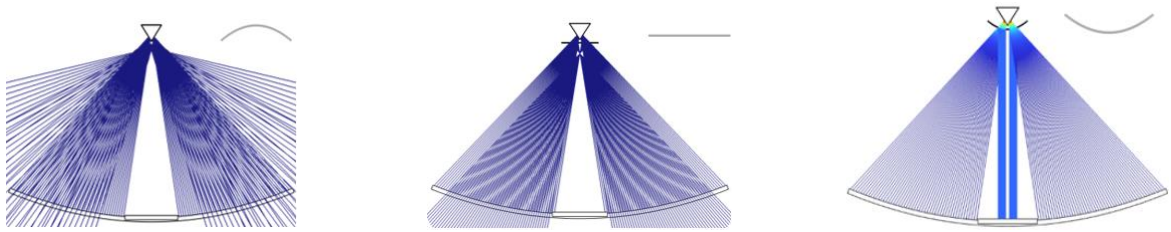

(a) (b) (c)

Figure 5. Ray tracing diagram for the SBS-based CPV-T collector with: (a) concave splitter, (b) flat splitter, and (c) convex splitter.

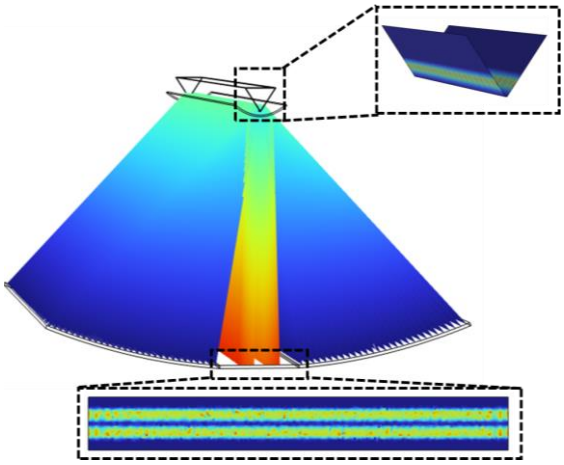

Figure 6. Ray tracing and flux distribution on the absorber for a convex SBS-based CPV-T collector.

3.4. Thermal modelling results

The transmitted fraction of 0.57 is then used in the 3-D model to account for the SBS component under the assumption that the component's ray-splitting properties remain constant throughout this study. This significantly reduced computational cost as the SBS component and optical simulation can be excluded from the 3-D model.

Heat transfer and fluid flow are then coupled into the 3-D optical model with transmission fraction to study the collector performance. The 3-D model is evaluated under the base case condition specified in Table 3. Under the base conditions, the primary PV-T module achieved an outlet HTF temperature (T_{out}) of 335 K (62 °C), average cell temperature (T_{cell}) of 329 K (56 °C), PV cell efficiency (η_{PV}) of 16 % and thermal efficiency (η_{th}) of 30 % whereas the secondary thermal absorber developed a thermal efficiency of 25%.

Table 3. Base case condition of the collector

Parameter	Symbol	Value	Unit
Solar irradiance	I_0	1000	W m^{-2}
Ambient temperature	T_{amb}	298	K
Windspeed	w	1	m s^{-1}
HTF mass flow rate	$\dot{m}$	0.001	kg s^{-1}
HTF inlet temperature	T_{in}	298	K

3.5. Sensitivity analysis

A parametric study on the effect of the operational parameters on the SBS-CPV-T collector performance is also conducted. The parameters in question are the base case parameters listed in Table 3. One parameter is varied at a time while the rest are kept constant at the base case value. The key performance indicators are the thermal and PV cell efficiency and outlet water temperature.

3.5.1. Effect of irradiance on collector performance

Figure 7a shows the variation in thermal and electrical efficiencies of the CPV-T collector with an increase in irradiance. The irradiance is varied from 200 to 1000 W m^{-2}. The increase in irradiance improves the thermal

performance of collectors, reaching as high as ~27% for the primary PV-T module (top absorber) and ~25% for the secondary thermal absorber (bottom absorber) at 1000 W m^{-2}. However, a decrease in electrical performance of the primary PV-T collector is observed with electrical efficiency reaching ~16% at 1000 W m^{-2}. The decrease in electrical efficiency can be attributed to an increase in cell temperature which also increases with an increase in irradiance. Figure 7b shows the variation of outlet water temperature for the primary PV-T module and secondary thermal absorber with an increase in irradiance. As the irradiance increases, the available solar energy that can be converted to heat also increases which subsequently leads to an increase in outlet temperature for both.

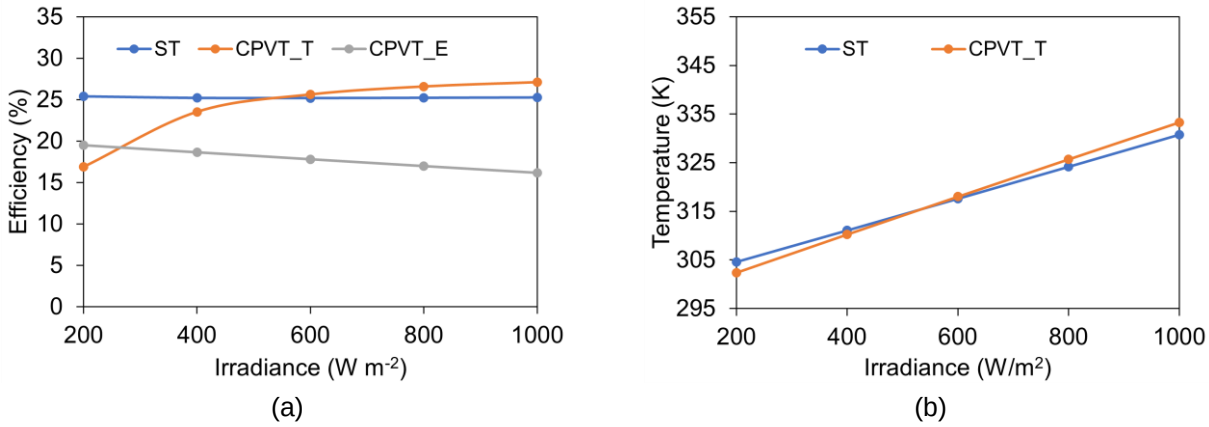

Figure 7. Effect of irradiance on: (a) thermal and electrical efficiency of CPV-T collector, (b) outlet water temperature.

3.5.2. Effect of flow rate on collector performance

Figure 8a shows the variation of thermal and electrical efficiencies of the collector with mass flow rate. As the mass flow rate increases, the larger fluid flow allows more heat to be recovered at the HTF. Hence, more heat is conducted away from the PV cell, causing cell temperature to drop. For a fixed irradiance of 1000 W m^{-2}, fixed inlet water temperature of 298 K and fixed ambient temperature of 298 K, the thermal efficiency of ~41% for the primary PV-T module and ~35 % for secondary thermal absorber is reported for a mass flow rate of 0.0045 kg s^{-1}. The corresponding electrical efficiency of ~17% is reported for the primary PV-T collector. However, the increased mass flow rate has an adverse effect on outlet water temperature. As the mass flow rate increases, the outlet water temperature decreases as shown in Figure 8b. For a mass flow rate of 0.0045 kg s^{-1} the outlet water temperature for the primary PV-T module is observed to be 310 K and the secondary thermal absorber is observed to be 308 K.

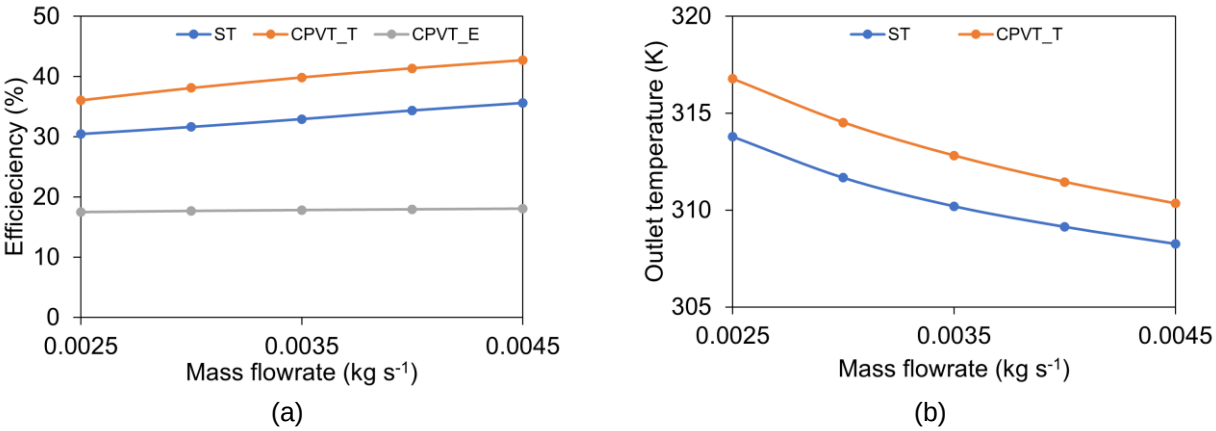

Figure 8. Effect of mass flow rate on: (a) thermal and electrical efficiency of SBS-based CPV-T collector, and (b) outlet water temperature of SBS-based CPV-T collector.

3.5.3. Comparison between the performance of CPV-T collectors with and without an SBS

The CPV-T collector with and without an SBS is also compared here. Figure 9 shows that only the flux within the spectral response of the cell will be utilised for electrical energy generation. The remaining flux will be converted to waste heat and contribute to an increase in cell temperature, which decreases PV cell efficiency. This analysis holds for both collectors. Figure 9a shows the variation of cell temperature and electrical efficiency with an increase in irradiance.

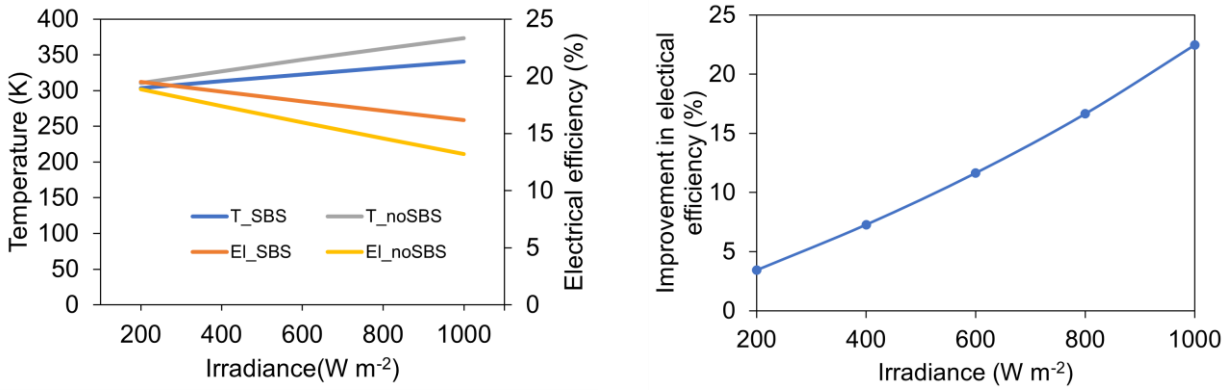

Figure 9. (a) Comparison of the effect of irradiance on electrical performance and cell temperature for SBS and non-SBS collectors. (b) Improvement in electrical efficiency for an SBS-based CPV-T collector compared to a conventional CPV-T collector.

The increase in irradiance leads to higher cell temperatures, which subsequently result in a decrease in electrical efficiency. For the non-SBS collector, the increase in cell temperature is as high as ~370 K at a mass flow rate of 0.001 kg s^{-1}, whereas for the SBS-based collector, the maximum temperature is ~340 K. The decrease in cell temperature allows a 22% electrical efficiency improvement, as shown in Figure 10b. The corresponding temperature distributions for the non-SBS and SBS-based collectors are shown in Figure 10. The comparison of performance between an SBS and a non-SBS collector is shown in Table 4.

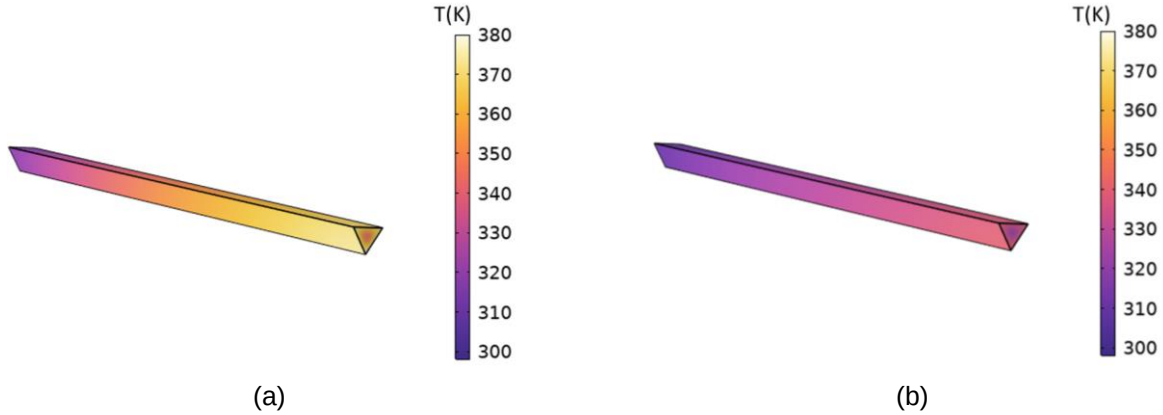

Figure 10. (a) Temperature distribution for non-SBS based CPV-TPV-T-T collector at 0.001 kg/s. (b) Temperature distribution for SBS based CPV-T collector at 0.001 kg/s.

Table 4. Performance of SBS & non-SBS CPV- T collectors.

CPV-T collector	Without SBS	With SBS
T_{cell}	373 K	340 K
T_{out} of HTF	361 K	333 K
η_{PV}	13 %	16 %
η_{th}	48 %	52 %

4. Conclusions

In this work, a comprehensive coupled optical-thermal model of the CPV-T collector integrated with an SBS has been developed. The SBS is specified to be a double-layer dichroic glass filter which transmits the solar spectrum between 500-1100 nm onto a primary PVT module and reflects the rest of the spectrum onto a secondary thermal absorber. Optical simulations were performed on concave, flat and convex profiles of the SBS integrated into a CPV-T collector. The results of these simulations showed that the convex profile directs the maximum part of the UV and IR spectrum on a secondary thermal absorber. Optical simulations also showed that the transmitted fraction from the SBS reaching the solar cell was 0.57, which was in line with other reported studies. Optical simulations were then coupled to the CFD model to estimate the electrical and thermal performance of the primary PV-T module and secondary thermal absorber. For a mass flow rate of 0.001 kg s^{-1}, wind speed of 1 m

s^{-1}, inlet water and ambient temperature of 298 K, the primary PV-T module attained a thermal efficiency of 30% and an electrical efficiency of 16%, whereas the secondary thermal absorber reached a thermal efficiency of 25%. In addition, a sensitivity analysis conducted on the SBS-based CPV-T collector showed that a lower solar irradiance and higher HTF mass flow rate enhance the PV cell efficiency. Finally, a comparative study conducted on CPV-T collectors with and without SBS showed that integration of an SBS lowered the cell temperature by ~33 °C, which translated to an improvement in electrical efficiency of ~22%.

Acknowledgement

This work was supported by the UK Engineering and Physical Sciences Research Council (EPSRC) [grant numbers EP/M025012/1, EP/R045518/1, and EP/S032622/1] and an Imperial College London EPSRC Impact Acceleration Account [grant number EP/R511547/1]. The work was also supported by the Royal Society under an International Collaboration Award 2020 [grant number ICA\R1\201302]. The authors would like to thank UK company Solar Flow Ltd. (www.solar-flow.co.uk). Data supporting this publication can be obtained on request from cep-lab@imperial.ac.uk. For the purpose of Open Access, the authors have applied a CC BY public copyright licence to any Author Accepted Manuscript version arising from this submission.

Nomenclature

g	Acceleration due to gravity (m s^{-2})
c	Speed of light (m s^{-1})
a	Area (m^2)
h	Convective heat transfer coefficient (W m^{-1} K^{-1})
GCR	Geometrical concentration ratio
q	Heat flux generated (W m^{-2})
d_h	Hydraulic diameter (m)
S	Incident radiation (W m^{-2})
I	Irradiance (W m^{-2})
m	Mass flowrate (kg s^{-1})
OCR	Optical concentration ratio
p	Perimeter (m)
P	Pressure (N m^{-2})
r	Reflection coefficient
Re	Reynolds number
c_p	Specific heat capacity (J kg^{-1} K^{-1})
T	Temperature (K)
k	Thermal conductivity (W m^{-1} K^{-1})
v	Velocity of the fluid (m s^{-1})
w	Wind speed (m s^{-1})

Subscript

amb	ambient
cell	solar cell
conc	concentrator
conv	convection
f	fluid domain
i	incident
opt	optical
out	outlet
PV	photovoltaic cell
rad	radiation
s	solid domain
SBS	spectral beam splitter
t	transmitted

Greek symbols

η	Efficiency
θ	angle
τ	Transmission
α	absorption
ε	emissivity
σ	Stefan-Boltzmann constant
μ	dynamic viscosity of the fluid
ρ	Density of the fluid

References

[1] Renewable Energy Agency, Renewable energy statistics 2022. Available at: <www.irena.org> [accessed 23.03.2023].
[2] Solanki C.S., Solar photovoltaics: fundamentals, technologies, and applications. PHI; 2015.
[3] Ayushi C., Sagnik C., Eswara P., Global solar water heater market. Available at: <www.alliedmarketresearch.com/solar-water-heater-market-A07957> [accessed 23.03.2023].
[4] Chandan, Suresh V., Iqbal S.M., Reddy K.S., Pesala B., 3-D numerical modelling and experimental investigation of coupled photovoltaic thermal and flat plate collector. Sol Energy 2021; 224:195-209.
[5] Herrando M., Wang K., Huang G., Otanicar T., Mousa O.B., Agathokleous R.A., Ding Y., Kalogirou S., Ekins-Daukes N.J., Taylor R.A., Markides C.N., A review of solar hybrid photovoltaic-thermal (PV-T) collectors and systems. Progress in Energy and Combustion Science 2023.
[6] Guarracino I., Mellor A., Ekins-Daukes N.J., Markides C.N., Dynamic coupled thermal-and-electrical modelling of sheet-and-tube hybrid photovoltaic/thermal (PVT) collectors. Appl Therm Eng 2016; 101:778-95.

[7] Guarracino I., Freeman J., Ramos A., Kalogirou S.A., Ekins-Daukes N.J., Markides C.N., Systematic testing of hybrid PV-thermal (PVT) solar collectors in steady-state and dynamic outdoor conditions. Appl Energy 2019; 240:1014-30.
[8] Huang G., Curt S.R., Wang K., Markides C.N., Challenges and opportunities for nanomaterials in spectral splitting for high-performance hybrid solar photovoltaic-thermal applications: a review. Nano Mater Sci 2020; 2(3):183-203.
[9] Herrando M., Ramos A., Zabalza I., Markides C.N., A comprehensive assessment of alternative absorber-exchanger designs for hybrid PVT-water collectors. Appl Energy. 2019; 235:1583-602.
[10] Ma T., Li M., Kazemian A., Photovoltaic thermal module and solar thermal collector connected in series to produce electricity and high-grade heat simultaneously. Appl Energy 2020; 261:114380.
[11] Chandan, Dey S., Iqbal S.M., Reddy K.S., Pesala B., Numerical modeling and performance assessment of elongated compound parabolic concentrator based LCPVT system. Renew Energy 2021; 167:199-216.
[12] Chandan, Dey S., Kumar P.S., Reddy K.S., Pesala B., Optical and electrical performance investigation of truncated 3X non-imaging low concentrating photovoltaic-thermal systems. Energy Convers Manage 2020; 220:113056.
[13] Chandan, Baig H., Tahir A.A., Reddy K.S., Mallick T.K., Pesala B., Performance improvement of a desiccant based cooling system by mitigation of non-uniform illumination on the coupled low concentrating photovoltaic thermal units. Energy Convers Manage 2022; 257:115438.
[14] Huang G., Wang K., Markides C.N., Efficiency limits of concentrating spectral-splitting hybrid photovoltaic-thermal (PV-T) solar collectors and systems. Light Sci Appl 2021; 10(1):28.
[15] Gorouh H.A., Salmanzadeh M., Nasseriyan P., Hayati A., Cabral D., Gomes J., Karlsson B., Thermal modelling and experimental evaluation of a novel concentrating photovoltaic thermal collector (CPVT) with parabolic concentrator. Renew Energy 2022; 181:535-53.
[16] Parthiban A., Reddy K.S., Pesala B., Mallick T.K., Effects of operational and environmental parameters on the performance of a solar photovoltaic-thermal collector. Energy Convers Manage 2020; 205:112428.
[17] Peacock J., Huang G., Song J., Markides C.N., Techno-economic assessment of integrated spectral-beam-splitting photovoltaic-thermal (PV-T) and organic Rankine cycle (ORC) systems. Energy Convers Manage 2022; 269:116071.
[18] Liang H., Su R., Huang W., Cheng Z., Wang F., Huang G., Yang D., A novel spectral beam splitting photovoltaic/thermal hybrid system based on semi-transparent solar cell with serrated groove structure for co-generation of electricity and high-grade thermal energy. Energy Convers Manage 2022; 252:115049.
[19] Zhang J.J., Qu Z.G., Wang Q., Zhang J.F., He Y.L., Multiscale investigation of the plasmonic solar cell in the spectral splitting concentrating photovoltaic-thermal system. Energy Convers Manage 2021; 250:114846.
[20] Yazdanifard F., Ameri M., Taylor R., Parametric investigation of a nanofluid-NEPCM based spectral splitting photovoltaic/thermal system. Energy Convers Manage 2021; 240:114232.
[21] Wingert R., O'Hern H., Orosz M., Harikumar P., Roberts K., Otanicar T., Spectral beam splitting retrofit for hybrid PV/T using existing parabolic trough power plants for enhanced power output. Sol Energy 2020; 202:1-9.
[22] Zhao X., Han X., Yao Y., Huang J., Stability investigation of propylene glycol-based Ag@ SiO2 nanofluids and their performance in spectral splitting photovoltaic/thermal systems. Energy 2022; 238:122040.
[23] Zhang J.J., Qu Z.G., Zhang J.F., MCRT-FDTD investigation of the solar-plasmonic-electrical conversion for uniform irradiation in a spectral splitting CPVT system. Appl Energy 2022; 315:119054.
[24] Calise F., Vanoli L., Parabolic trough photovoltaic/thermal collectors: design and simulation model. Energies 2012; 5(10):4186-208.
[25] Frei W., Introducing the ray optics module COMSOL Blog. Available at: <www.comsol.com/blogs/introducing-ray-optics-module> [accessed 27.02.2023].
[26] Parthiban A., Mallick T.K., Reddy K.S., Integrated optical-thermal-electrical modelling of compound parabolic concentrator based photovoltaic-thermal system. Energy Convers Manage 2022; 251:115009.
[27] Wang K., Herrando M., Pantaleo A.M., Markides C.N., Technoeconomic assessments of hybrid photovoltaic-thermal vs. conventional solar-energy systems: Case studies in heat and power provision to sports centres. Appl Energy 2019; 254:113657.
[28] Bergman T.L., Bergman T.L., Incropera F.P., Dewitt D.P., Lavine A.S., Fundamentals of heat and mass transfer. John Wiley & Sons; 2011.
[29] Tang F., Li G., Tang R., Design, and optical performance of CPC based compound plane concentrators. Renew Energy 2016; 95:140-51.
[30] Bahaidarah H.M., Gandhidasan P., Baloch A.A., Tanweer B., Mahmood M., A comparative study on the effect of glazing and cooling for compound parabolic concentrator PV systems–Experimental and analytical investigations. Energy Convers Manage 2016; 129:227-39.